

See discussions, stats, and author profiles for this publication at: <https://www.researchgate.net/publication/263960182>

Three-Dimensional Water Vapor Visualization in Porous Packing by Near-Infrared Diffuse Transmittance Tomography

ARTICLE in INDUSTRIAL & ENGINEERING CHEMISTRY RESEARCH · FEBRUARY 2012

Impact Factor: 2.59 · DOI: 10.1021/ie202023t

CITATIONS

2

READS

19

6 AUTHORS, INCLUDING:



Daniel Luis Abreu Fernandes

Uppsala University

25 PUBLICATIONS 157 CITATIONS

[SEE PROFILE](#)



Jacinto Sa

Paul Scherrer Institut

43 PUBLICATIONS 406 CITATIONS

[SEE PROFILE](#)



Farid Aiouache

Lancaster University

22 PUBLICATIONS 198 CITATIONS

[SEE PROFILE](#)

Three-Dimensional Water Vapor Visualization in Porous Packing by Near-Infrared Diffuse Transmittance Tomography

Méabh Nic An tSaoir,[†] Daniel Luis Abreu Fernandes,[‡] Jacinto Sá,[§] Kuniyuki Kitagawa,[⊥]
Christopher Hardacre,[†] and Farid Aiouache*,[†]

[†]Queen's University Belfast, School of Chemistry and Chemical Engineering, Stranmillis Road, Belfast, BT9 5AG, Northern Ireland

[‡]Department of Chemistry, University of Aveiro, Campus de Santiago, 3810-193 Aveiro, Portugal

[§]ETH Zürich, Chemistry and Bioengineering, Wolfgang-Paulistrasse 10, 8093 Zürich, Switzerland

[⊥]Ecotopia Science Institute, Nagoya University, Chikusa-ku 464-8603, Nagoya, Japan

ABSTRACT: This work presents a procedure based on two-dimensional and three-dimensional spatially resolved near-infrared imaging to observe temperature and composition maps in gas–solid packed beds subjected to effects of aspect ratio and nonisothermal conditions. The technique was applied to the water vapor flow in a fluidized bed and a packed bed reactor and confirmed uneven water vapor flow channeling and temperature distributions in the core packed bed and in the vicinity of the wall due to flow maldistribution. In addition, the heat uptake and local cross-mixing were experimentally ascertained.

1. INTRODUCTION

Among the various reactor types used in the laboratory, continuous flow differential reactors are particularly flexible as they offer both temporal and spatial information on heat, mass, and flow dynamics leading to more understanding of the isotropic distributions changes at various spatiotemporal scales. Measurements are unfortunately carried out using one or more analytical techniques most of which tend to be “single point” techniques. These techniques have helped one to understand fundamental phenomena using simplified concepts relying on pseudohomogeneous descriptions of underlying events where the integral and differential quantities such as diffusion rates, process conversions, and selectivity are obtained by monitoring the inlet and outlet values or by multiple experiments in which invasive probes are placed at different locations. Recent developments in spatially resolved techniques have allowed magnetic resonance imaging (MRI),¹ X-ray,² neutron,³ and laser spectroscopy⁴ to measure local properties which exhibit anisotropic distributions such as dispersion coefficients in liquid–solid reactors at millimeter resolution, achieving thus rapid access to scalar data of chemical kinetics and associated mass transfers in a single experiment. Unfortunately, these techniques were revealed to be not sufficiently mature to be applied to gas–solid processes, due to the inherently weak signals retrieved from the gaseous phase.⁵ Nevertheless, optical techniques are increasingly cited in both open and industrial literature, being boosted by rapid developments in tunable lasers and single or 2D array detectors and leading to experiments being performed at high spatiotemporal resolutions.^{5,6}

In the present work, two experimental procedures based on spatially resolved NIR imaging are presented; their capabilities are demonstrated by observing water vapor (H_2O_v) flow subjected to entrance effects, to tube to particle aspect ratio, and to nonisothermal conditions. The first technique, which involves the use of NIR broadband light, interference optical filters centered on absorbing and nonabsorbing wavelengths of H_2O_v , a Vidicon NIR camera, and single back-projection of collected images, is applied

to 2D imaging of gas–solid fluidized bed reactor with a low aspect ratio of tube to particle diameters (D_t/d_p).^{7,8} The second technique uses a tunable diode laser, focal planar array detector, and tomographic reconstruction from multiple back-projections and is applied to 3D imaging of H_2O_v flow in a packed bed reactor filled with a silica gel where the hydrogen isotopic exchange (HIE) reaction occurs. These techniques take advantage of rapid developments in fiber optics and high-speed electronics which have greatly reduced the experimental difficulty of tomography, to the extent that a relatively large number of projections can be implemented and recorded in a few minutes.

2. MATERIAL AND METHODS

2.1. 2D Imaging. The first technique for 2D imaging is introduced in Figure 1 which shows a quartz reactor (0.02 m I.D. and 0.5 m in height), made of fused silica and covered with a carbon-based ribbon to simulate blackbody radiative heating by the side electrical heaters. Two lateral windows with an aperture of $0.009 \times 0.10 \text{ m}^2$ were kept uncovered for side observations. An inner tube (0.008 m I.D.) which was filled with a packed bed (0.02 m height) was inserted at the center of the reactor and whose nozzle was located at 0.01 m above the bottom base of the lateral window. The packing particles were prepared by an incipient wetness method using an aqueous solution of Ce ($(\text{NH}_4)_2(\text{NO}_3)_6$) (Wako Co.) and SiO_2 (Aerosil, 380 m^2/g , SIGMA-Aldrich, Inc.) as detailed in our previous work.⁷ In order to force flow channeling, a small ratio of tube to particle diameter (D_t/d_p) was selected. Particles narrowly sieved between 0.00045 and 0.0005 m with an average diameter of approximately 0.000475 m were used. NIR imaging of H_2O_v flow in N_2 flow was conducted using a NIR

Special Issue: CAMURE 8 and ISMR 7

Received: September 8, 2011

Revised: February 3, 2012

Accepted: February 7, 2012

Published: February 7, 2012



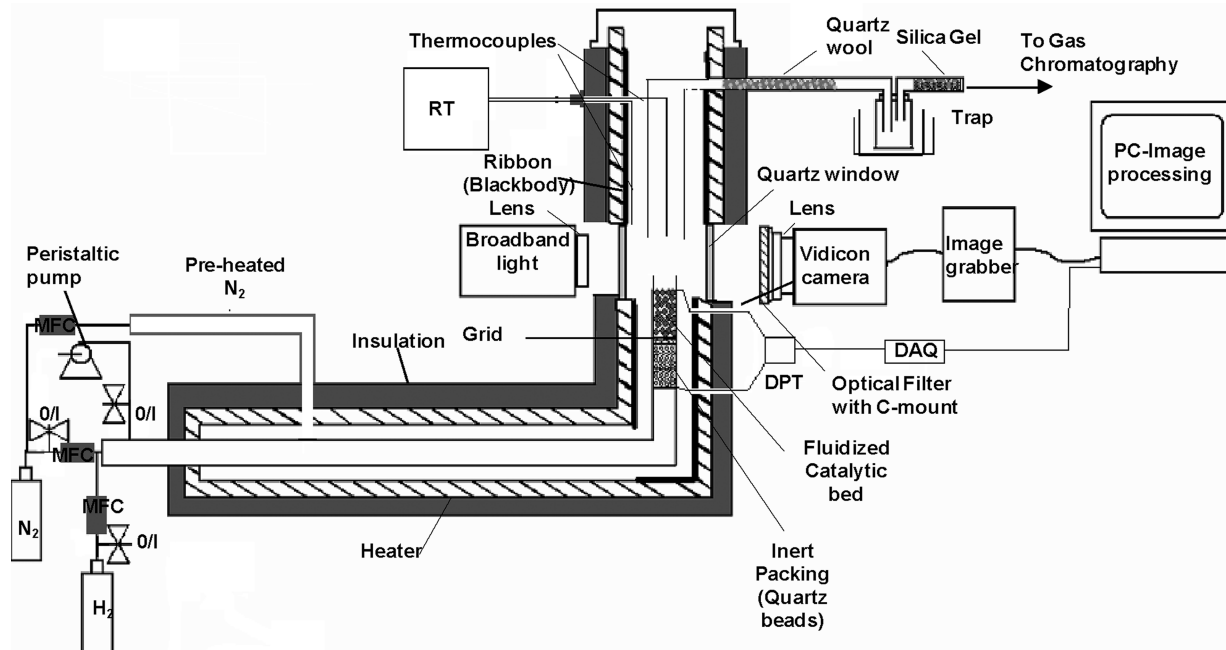


Figure 1. Experimental setup. RT: Regulator of temperature; I/O: ON/OFF valves; MFC: mass flow controller; DAQ: data acquisition; DPT: differential pressure transducer.

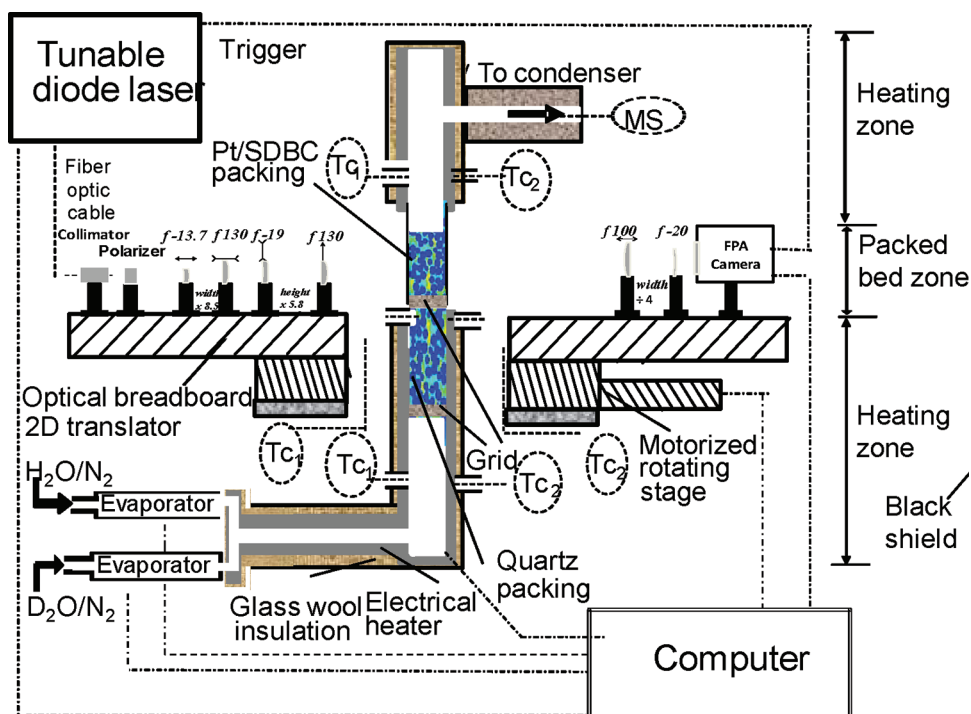


Figure 2. Scheme of the whole tomography apparatus: Evaporator (Bronkhorst) = Mass flow controller (N₂), air-actuated switching valve, distilled water bath; H: Humidity sensor; TC₁ = Thermocouples (monitoring), TC₂: Thermocouples connected to programmable temperature controllers; MS: Mass spectrometer; Optics = details of optics are shown in Figure 1b; Tunable diode laser: Lock-in monomode connected to FPA camera; Quartz packing: prepacked bed mixer, Pt/SDBC packed bed = Height:14 cm; visible aperture by NIR camera: 1.20 × 1.82 cm². Monomode fiber-optic cable connected to a collimator with a top-hat beam shaper (size: 5 mm); polarizer, two couple of cylindrical lenses of focal points f (mm): f=13.7, f=130 and f=19, f=130, trans-illuminated backed bed and couple of lens (f=100, f=20) and intercepted beam size by FPA detector.

Vidicon camera (Hamamatsu Photonics, C2741) with a sensing wavelength range of 400 to 2200 nm and positioned 0.02 m away from the quartz windows. Two optical filters (Andover) centered at 1390 and 1230 nm were used for H₂O_v absorbing and nonabsorbing regions, respectively.

2.2. 3D Imaging by NIR Tomography. The second technique for 3D imaging of distributions of temperature and composition inside and above a packing is shown in Figure 2. The tube was made of fused quartz of 9 mm I.D. and filled with 0.75 g of hydrophobic Pt/SDBC resin (particle size of 80–100

μm , average pore size of 110–175 \AA , surface area of 900 $\text{m}^2 \text{ g}^{-1}$, and 2% platinum, prepared by impregnation, as reported by Paek et al.⁹). Typically, a D_2O_v composition of 12.0 mol % (RH of 60.1%) was introduced by bubbling a mixture of H_2 (20 mol % in N_2) at 338 $\text{cm}^3 \text{ min}^{-1}$ and temperature of 333 K using a controlled evaporator mixer (Bronkhorst). All pre- and postpacked tube pipes were insulated and heated to the operating temperature. Outlet products were measured by Pfeiffer Omistar GSD O mass spectrometer equipped with a quadrupole analyzer. The pressure of the ionization chamber was set roughly to 10^{-2} mbar. Fragmentation factors were calculated by adding all the possible mass to charge ratios (m/z) and normalized by the highest signal that can be expected for each chemical species (H_2O , D_2O , and HDO) based on the NIST database. Sensitivity coefficients for each species were determined by computing the signal to concentration ratios normalized to the signal (m/z : 36) to concentration ratios of the internal standard Argon. The entire experimental set-up was enclosed within a black-shielded Perspex box and purged of excess moisture by dry nitrogen.

The tomography technique relied on 2D projected images from parallel scanning. An NIR, polarized, CW tunable laser source ($12.0 \times 18.2 \text{ mm}^2$ size) and a focal planar array (FPA) NIR detector (Mosir 950 detector, Intervac, 1024×256 pixels, $26 \times 26 \mu\text{m}^2/\text{pixel}$, 1 MHz, 15 scans/test) were coupled to acquire a single projection and to measure both the transmission data through the H_2O_v media and the diffused transmission data through the packed bed. The CW laser (Santec TSL-510) with a line width of 1 MHz, a modulating range from 1340 to 1440 nm, scanning speed of 100 nm s^{-1} , and an output power of 4 mW was tuned to the high-extinction frequencies of H_2O_v or HDO_v . D_2O_v was not considered as it shows negligible extinction in the modulated range used. Motion control of the optical stage was achieved by a servo-motor which allowed 2D translations and rotation around the central axis of the packed bed. The tomographic reconstruction was designed for the purpose of simultaneous measurements of temperature and composition, using the adaptive algebraic reconstruction technique (AART). AART reconstructed on a discretized domain a 3D object function, $f(x,y,z)$, of unit coordinates (i,j,k). The object function was modeled as an array of discrete unknown voxels which resulted from a parallelepiped grid which was superimposed on the function of dimension $m \times m \times N$, providing a total number of voxels: $M = N \times m^2$. The object function was modeled as an array of discrete unknown voxels, leading to a system of equations.

$$\sum_{j=1}^M w_{ij} f_i = p_i \quad i = 1, 2, \dots, N \quad (1)$$

Here, w_{ij} is the weighting factor of the contribution of the j -th voxel to the i -th measurement; N is the total number of projection rays; and M is the total number of voxels. The numerical value of the weighting factor w_{ij} is equal to absorbance, Abs, or absorbance ratio, R , of the 3D image voxel (k -th, j -th pixels) intercepted by the i -th hyperplane ray. The Kaczmarz iterative method was then used for solving algebraic equations.¹⁰

$$f_j^l = f_j^{l-1} - \frac{f_j^{l-1} \cdot w_{ij}}{\sum_{j=1}^N w_{ij} \cdot (f_j^{l-1} \cdot w_{ij})} \left(\sum_{j=1}^N w_{ij} f_j^{l-1} - p_i \right) \quad (2)$$

Here, $f^{k-1} \cdot w_i$ is the dot product and k is the iteration index. Reconstruction of cross-sectional images or slice matrixes was repeated for each subsequent cross-sectional matrix until the 3D local absorbance ratios, R , for temperature reconstructions, and the local absorbance, Abs, for composition reconstructions, were obtained for the packing and the above packing regions of the packed cylinder. The local absorbance ratio and local absorbance were converted to temperature and composition using eqs 9 and 10.

3. RESULTS AND DISCUSSION

3.1. Two Dimensional (2D) Visualization of H_2O_v Flow at the Exit of a Fluidized Bed Reactor. The validation test of 2D imaging was carried out by imaging the steady-state dispersion of H_2O_v in N_2 using two cocurrent flows. H_2O_v was injected from the inner empty tube at superficial velocity of 0.05 ms^{-1} , composition of 1.35 mol/m^3 whereas pure N_2 was blown in the outer tube at similar velocity. The flow of H_2O_v blowing from the nozzle was visualized by directing the diffuse broadband light across the exit of the well-defined nozzle before being intercepted by the NIR camera. Figure 3 shows the distribution of transmittance of H_2O_v blowing out of the tube at 873 K and mixing with the outer flow (N_2) and illustrates lower

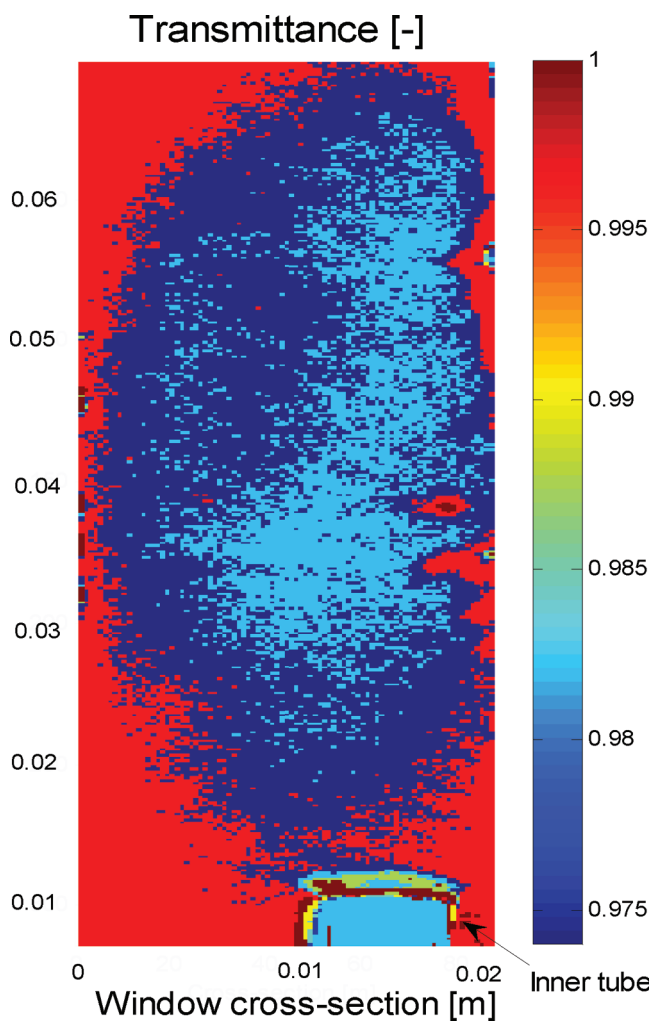


Figure 3. Integral transmittance of water vapor at the nozzle exit. Water vapor concentration: 1.35 mol/m^3 in N_2 ; temperature: 873 K; and pressure: 101.3 kPa. Inner flow ($\text{N}_2 + \text{H}_2\text{O}$): 150 mL min^{-1} ; outer flow (N_2): 790 mL min^{-1} .

values of integral transmittance along the central axis due to higher optical paths than those at lateral sides. Values of transmittance in Figure 3 at a position of 2 mm above the inner tube and normalized to actual optical path are shown in Figure 4.

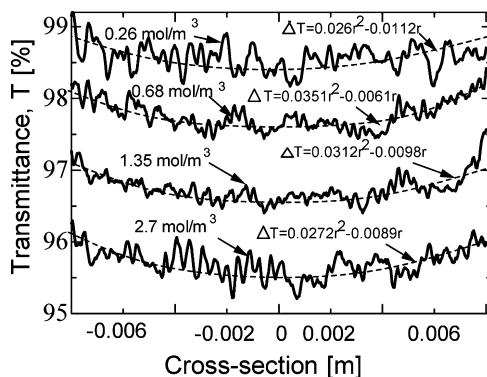


Figure 4. Cross-sectional transmittance as a function of concentration of water vapor normalized to actual light path trans-illuminating the flow, at 2 mm above the inner tube; temperature: 873 K; and pressure: 101.3 kPa; inner flow: ($N_2 + H_2O$) 150 mL min⁻¹; outer flow (N_2): 790 mL min⁻¹.

In addition, transmittance profiles for further concentrations of H_2O_v of 2.7, 1.35, 0.68, and 0.26 mol/m³ are illustrated in Figure 4. Lower values of transmittance are still observed in the core center of the cross-sectional path than at the sides, whereas similar cross-sectional values of transmittance, and by inference concentrations, were expected to be observed on the blowing flow from the inner tube. These deviations in transmittance along the radial coordinate of the inner tube as illustrated in Figure 4 were used therefore for transmittance normalization in the static and fluidized beds in the following section.

The minimum bubbling velocity (U_{mb}) and minimum fluidization velocity (U_{mf}) were determined from a decreasing velocity run, while U_c was determined from an ascending velocity run. Figure 5 shows the pressure difference over the bed as a

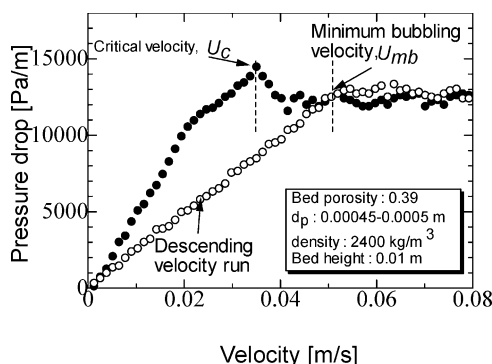
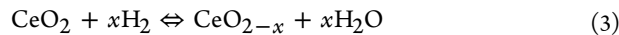


Figure 5. Pressure drop over the fluidized catalytic bed as a function of fluid velocity.

function of fluid velocity at 298 K. The pressure difference profile is similar to the profiles of group B solids of the Geldart classification. A small pressure overshoot and small oscillations were observed at a U_c value of 0.04 ms⁻¹ while the U_{mb} and minimum fluidization velocity U_{mf} were found at similar values of 0.05 ms⁻¹.

Next, the fluidized bed presented herein was operated at static and minimum bubbling conditions in order to ensure two

types of radial porosity profiles. Static bed operations were performed in a pseudostatic state, which was localized by the so-called critical superficial velocity (U_c) coinciding with maximum values of pressure drop overshoots. The fluidized bed operations were run at minimum bubbling velocity (U_{mb}), with the two types of operation ensuring two different radial porosity profiles. Compared with porosity profiles at U_c , whose values are high in the vicinity of the wall and low in the core bed, porosity profiles at U_{mb} develop opposite concentration gradient profiles along the radial coordinate, as bubbling occurs preferentially in the central region of the bed.¹⁰ The reduction of ceria–silica as illustrated by eq 3 was investigated.



Herein, x is the mole number of oxygen vacancies per mole of reduced ceria. This reaction was selected because ceria–silica mixture contains oxygen and anionic vacancies whose diffusion rates vary along the progress of the reduction which can be followed by 2D imaging of H_2O_v .¹¹ At low conversions, the kinetics is dominated by surface reactions of hydrogen activation, anionic vacancies formation, and water release. At high conversions, however, a slow bulk diffusion of oxygen occurs and the wall effect on channeling should therefore vary along with the progress of the reaction. In a single experiment herein, the packing bed was heated in an N_2 atmosphere at 873 K until a thermal equilibrium was reached. Then, hydrogen (concentration of 1.35 mol/m³) was charged, and averaged cross-sectional transmittance response, normalized to optical path, positioned at 0.002 m above the inner tube was collected as a function of time by NIR imaging. Cross-sectional concentration profiles of H_2O_v inside the packed bed as a function of the reduction time and two gas velocities U_c and U_{mb} are shown in Figure 6a,b, respectively. An initial period of fast

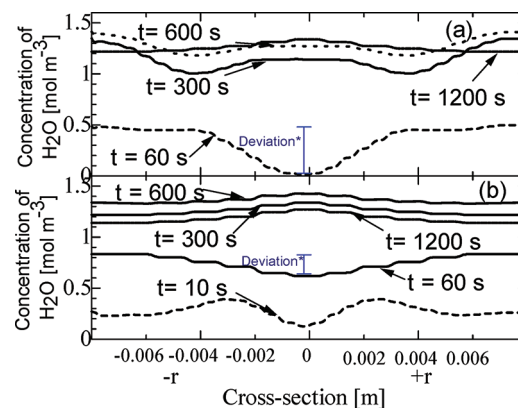


Figure 6. Cross-sectional mole fractions reconstructed from the line of sight integral transmittance positioned at 2 mm above the nozzle during the catalytic reduction of ceria-based ceria–silica, panel (a) at U_c and panel (b) at U_{mb} . Hydrogen concentration: 1.35 mol/m³ in N_2 ; temperature: 873 K; and pressure: 101.3 kPa. *Example of concentration deviations at 60 s between the center and the wall of the inner tube at U_c and U_{mb} .

release of H_2O_v lasted approximately 600 s, and there was a second period which was slow but associated with a long release time. Unlike Figure 6b, Figure 6a shows higher concentrations of H_2O_v in the vicinity of the wall of the inner tube than in the core center of the bed during the period of fast release of water of 600 s. For this first period, as the reaction continued, the concentration extended from the wall

to the core and covered the whole of the cross-section of the inner reactor. This behavior resulted from the high velocities near the wall, which led to lower residence times of hydrogen compared to the core of the bed. Flow channeling in the vicinity of the wall did occur when the bed was run at U_c . Flow channeling at the wall was not observed at slightly higher velocities such as the U_{mb} as seen in Figure 6b. In accordance with multiple works on porosity profiles in fluidized beds under bubbling operations,^{12,13} the gas velocity served essentially to adjust the flow rate and volume fraction of the bubbles in the core of the bed and accordingly induced an increase in the core porosity; while in contrast to this, the local velocity in the vicinity of wall remained nearly constant. Figure 7a,b shows

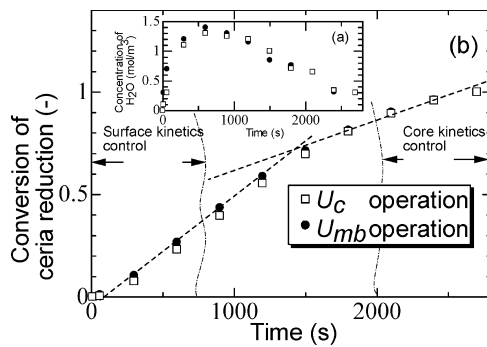


Figure 7. Transectionally averaged concentration of water vapor (a) and conversion of catalyst reduction (b) at U_c and U_{mb} operations. Hydrogen concentration: 1.35 mol/m³ in N₂; temperature: 873 K; and pressure: 101.3 kPa.

profiles of both trans-sectionally averaged concentration of H_2O_v and respective conversions of catalyst reduction at U_c and U_{mb} operations. Both figures show that the kinetics of reduction was slightly faster at U_{mb} operation compared with U_c operation for the first 600 s of reaction course where the kinetics was under surface control whereas the kinetics was the same at U_{mb} and U_c under diffusion control at the reaction course beyond 1200 s.

The 2D NIR imaging allowed existing models of thin fixed bed reactors to be extended to pseudostatic bed operations. When hydrogen was passed through the bed at U_c , it just percolated through the void spaces between the particles. When the velocity was increased beyond pseudostatic-state operation to say U_{mb} , the buoyancy of the upward moving flow counterbalanced both the weight of the bed and the viscous forces in the vicinity of the wall. The technique however did not show local changes which would require a 3D imaging measurement as explained in the following section.

3.2. 3D Imaging by NIR Tomography of Transient H_2O_v and Temperature Profiles during the Hydrogen Isotopic Exchange Reaction in Pt/SDBC Resin-Packed Bed Reactor of Low Aspect Ratio. Compared with the 2D imaging which shows the anisotropic changes along the radial direction, the 3D imaging is expected to show the changes in both radial and angular directions leading to local information on heat, mass, and flow dynamics. The Pt/DSBC resin reactor with a small aspect ratio was used in conjunction with the intraparticle diffusion in Pt/DSBC catalyst as reported by Roland et al.¹⁴ The 3D distributions of derived transient changes of H_2O_v , HDO_v , and temperature during the HIE

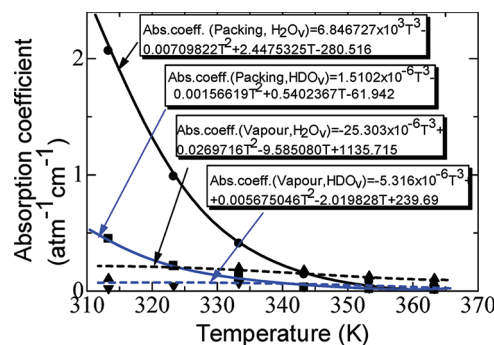


Figure 8. Absorption coefficients of H_2O_v and HDO_v with temperature at 1380.685 and 1390.24 nm, respectively, in both the packing phase and the vapor phase above the packing.

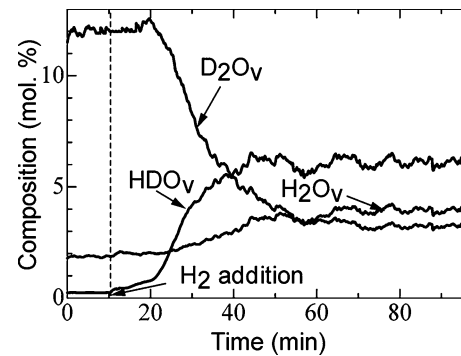
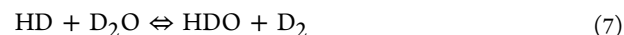


Figure 9. HIE dynamics of HDO_v , H_2O_v , and D_2O_v compositions at the exit of the packed bed reactor obtained by mass spectrometry; packing height: 14 mm; particle size 0.7 mm (AR: 13); wall temperature: 333 K; D_2O_v (inlet): 12 mol %; H_2 (inlet): 25 mol %; N_2 (inlet): 63 mol % and N_2 flow rate: 250 cm³ min⁻¹.

reaction of heavy water vapor (D_2O_v) and hydrogen gas, as illustrated by eqs 4–8, are described by NIR tomography.



The extinction coefficients of H_2O_v or HDO_v across the packing section and the empty section above the packing of the cylindrical packed bed were obtained using a squared quartz cell of 10 × 10 mm² cross-section and 100 mm height, which was half-filled with the SDBC packing. The pair of lines of H_2O_v at 1358.412 and 1380.685 nm was found to be a good fit in terms of temperature sensitivity, since it offers a difference in the lower-state energy ($E_2 - E_1$) of 283 cm⁻¹, a line strength ratio at reference temperature ($S_1(T_0)/S_2(T_0)$) of 1.19, and a good separation from lines of HDO_v . The modified Beer–Lambert law was used for concentration measurements, and temperature was measured by computing the absorbance ratio for two temperature-dependent transition lines.^{15–19}

Assuming that the offset value was weakly dependent on the changes of attenuation wavelength and the brightness of a visualized image was proportional to the laser light intensity I_λ

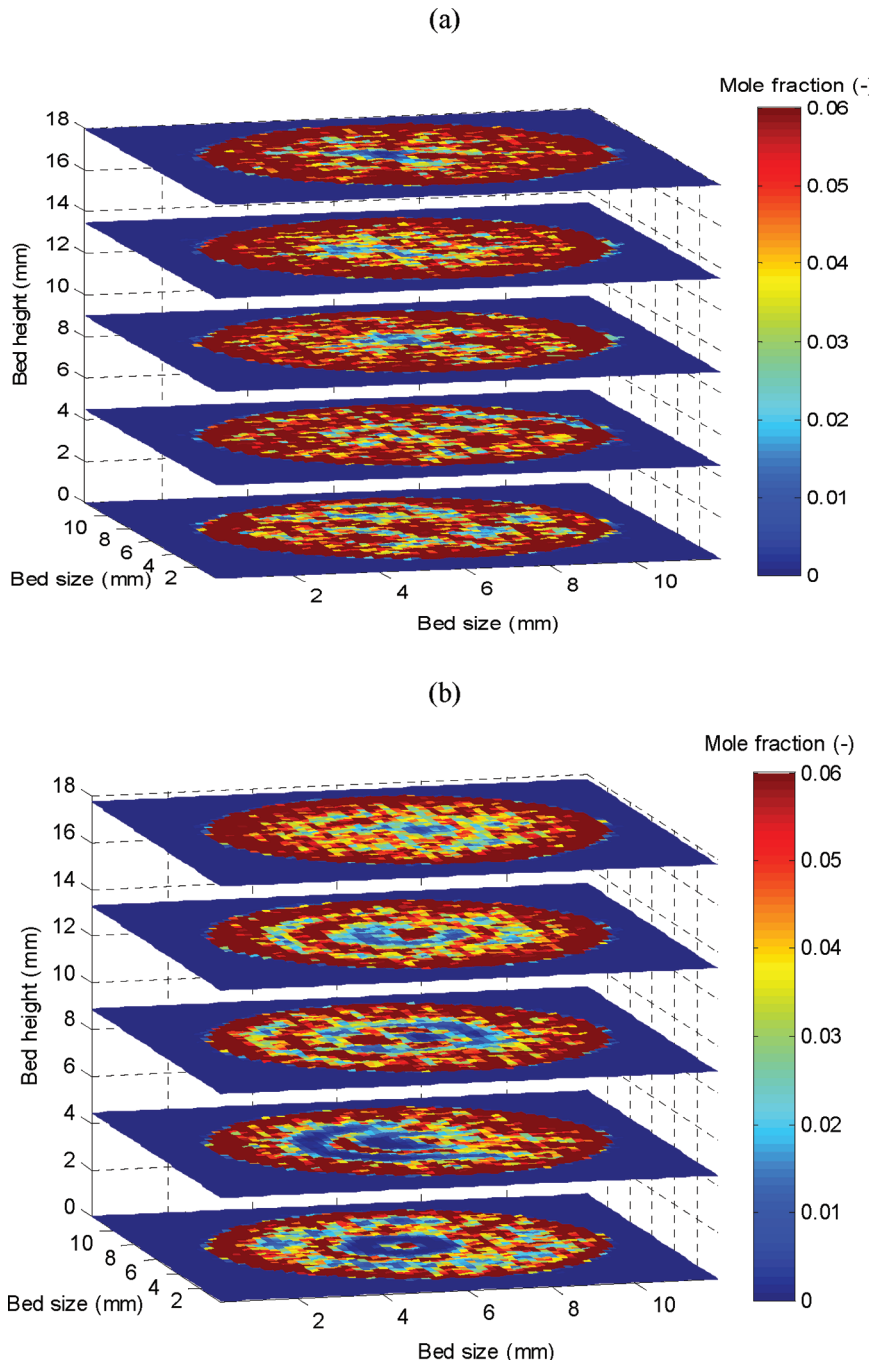


Figure 10. HIE by spatial distributions of HDO_v and H₂O_v compositions of five cross-sectional layers located at equal distance from the bottom of the packing to the top of the vapor phase above the packing; (a): HDO_v; (b): H₂O_v; packing height: 14 mm; particle size 0.7 mm (AR: 13); wall temperature: 333 K; D₂O (inlet): 12 mol %; H₂ (inlet): 25 mol %; N₂ (inlet): 63 mol % and N₂ flow rate: 250 cm³ min⁻¹.

that trans-illuminated by a straight propagation the packed bed, the composition of H₂O_v or HDO_v was calculated by eq 9

$$\text{Abs}(T, \lambda) = \varepsilon(T, \lambda) \int C dl \quad (9)$$

where ε is the absorption coefficient without scattering through the packing, l is the forward optical path length, C is the uneven composition of H₂O_v or HDO_v across the packing, and Abs is the integral absorbance. The coefficients ε of H₂O_v and HDO_v were measured at similar wavelengths as those above the packing, ca. 1380.685 and 1390.24 nm, respectively,

temperature ranging from 313 to 363 K, and fitted to a polynomial model as a function of temperature. Figure 8 illustrates the experimental absorption coefficients ε in the packing and above the packing for H₂O_v and HDO and the polynomial fits with temperature.¹⁹

Local temperature was measured by computing the absorbance ratio, R , for two temperature-dependent transition lines.^{17,18}

$$R = \frac{S_1(T_0)}{S_2(T_0)} \exp \left[-\frac{hc(E_1 - E_2)}{k} \left(\frac{1}{T} - \frac{1}{T_0} \right) \right] \quad (10)$$

where $S_i(T_0, \lambda_i)$ is the line strength of the transition centered at line wavelength λ_i for a reference temperature T_0 , taken at 296 K; h is Planck's constant; c is the speed of light; k is Boltzmann's constant; E_i is the lower-state energy; and T is the gas temperature (K).

The validation tests were demonstrated in a previous work where the 3D imaging results were compared with results from a thermocouple and mass spectrometer placed at the empty section above the packed bed.¹⁹ The averaged relative deviations in H_2O_v composition and temperature to data obtained by mass spectrometry and thermocouple for full ranges of 1 to 6 mol % and 323 to 353 K were 16.1% and 18.3%, respectively.

The HIE reaction test was performed on a packed bed of an aspect ratio (AR) of 13, i.e., particle size of 0.7 mm, inlet and wall temperatures of 333 K, and flow rate of $250 \text{ cm}^3 \text{ min}^{-1}$, to assess the changes of temperature and composition distributions with time in the packing and above the packing of the packed bed, which would be caused by the confining wall. Figure 9 shows transient composition profiles of the water isotopomers H_2O_v , D_2O_v , and HDO_v measured by the mass spectrometer at the exit of the packed bed at inlet compositions of D_2O_v and H_2 of 12.0 and 25.0 mol % in N_2 , respectively, and at a temperature of 333 K. The steady-state compositions were achieved after 50 min. The inlet D_2O_v was subject to H_2O_v intrusion from the surrounding environment, ca. 1.7 to 1.8 mol %, in all experiments.

The derived composition profiles of HDO_v and H_2O_v and by NIR imaging with time were examined, as shown by Figure 10a,b, respectively, at steady-state operations. Each figure shows composition maps of five selected cross-sectional layers, located at equal distances from the bottom of the packing to the top of the vapor phase above the packing, where the four bottom layers belong to the packing section and the top layer to the empty section above the packed bed. H_2O_v and HDO_v compositions decreased particularly toward the core of the bed. The composition changes in the radial and angular directions of H_2O_v and HDO_v were up to 6 mol % in the packing

and the empty section above the packing. High compositions of both H_2O_v and HDO_v are located near the wall, and lower compositions are distributed randomly in the core center of the bed. HDO_v compositions are more pronounced than respective H_2O_v compositions which are in agreement with the higher kinetics of HDO_v formation obtained by mass spectrometry in Figure 9. These uneven distributions indicate that the local flow was stagnant, circulating or channeling between the resin particles.

The temperature profiles with time are shown by Figure 11. The hot areas expended particularly toward the core of the bed. In addition, changes in temperatures were up to 10 K throughout the packing and the empty space above the packing. The colder zones are closer to the wall where convective heat transfer dominates owing to a larger porosity in contact with the wall. It can be seen that the average wall temperature from the bottom to the top of the packed bed decreased as larger hot zones are displayed at the inlet. The effectiveness of wall heating of the packed bed can, therefore, be assessed qualitatively by observing actual maps in the vicinity of the wall and in the core packing. The decrease in temperature in the area near the wall and small changes in the temperature in the area toward the center demonstrate inefficient heat transfer from the wall to the packing. Hot zones, therefore, correspond to the situation where the flow velocity was uniform along the axial and radial directions, while cold zones reflect a minimal flow velocity, resulting in a reduced energy transfer between the wall and the packing.

4. CONCLUSION

This study demonstrated that NIR imaging can be extended to actual behavior of flowing gases by measuring the 2D and 3D distributions of composition and temperature at the exit of a packed bed or inside a weakly scattering packed bed reactor, subject to wall effects, mass transfer resistance, and non-isothermal conditions. H_2O_v and its isotope HDO_v were used owing to their high absorption coefficient in NIR. The extension

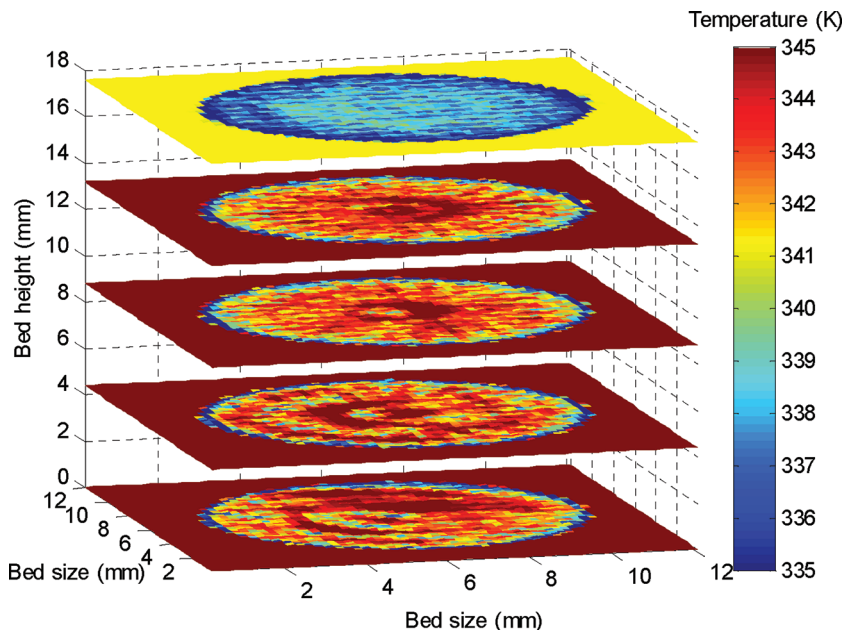


Figure 11. HIE by spatial distributions of temperature of five cross-sectional layers located at equal distance from the bottom of the packing to the top of the vapor phase above the packing; packing height: 14 mm, particle size: 0.7 mm (AR: 13); wall temperature: 333 K; D_2O_v (inlet): 12 mol %; H_2 (inlet): 25 mol %; N_2 (inlet): 63 mol % and N_2 flow rate: $250 \text{ cm}^3 \text{ min}^{-1}$.

to common gases such as CO, CO₂, and NO_x, which are known to exhibit low absorption coefficients compared with H₂O_v and HDO_v, is ongoing, using a suitable design to make NIR tomography sensitive to low compositions. Flow maldistribution and the dynamic lag between the near-wall compositions were observed. In addition, temperature was distributed unevenly, particularly toward the core which suggests that the convective transfer was also not effective in both the fluidized bed at pseudo-critical conditions and in the packed bed reactor.

AUTHOR INFORMATION

Corresponding Author

*E-mail: f.aiouache@qub.ac.uk.

Notes

The authors declare no competing financial interest.

REFERENCES

- (1) Rigby, S. P.; Gladden, L. F. NMR and fractal modelling studies of transport in porous media. *Chem. Eng. Sci.* **1996**, *51* (10), 2263.
- (2) Roels, S.; Carmeliet, J. Analysis of moisture flow in porous materials using microfocus X-ray radiography. *Int. J. Heat Mass Transfer* **2006**, *49*, 4762.
- (3) Asano, H.; Nakajima, T.; Takenaka, N.; Fujii, T. Visualization of the hygroscopic water distribution in an adsorbent bed by neutron radiography. *Nucl. Instrum. Methods Phys. Res., Sect. A* **2005**, *542*, 241.
- (4) Cai, C. B.; Han, Q. J.; Tang, L. J.; Xu, L.; Jiang, J. H.; Wu, H. L.; Yu, R. Q.. Studying the uptake of aniline vapour by active alumina through in line monitoring a differential adsorption bed with near-infrared diffuse reflectance spectroscopy. *Adsorption* **2009**, *15*, 23–29.
- (5) Nadeau, P.; Berk, D.; Munz, R. J. Measurement of residence time distribution by laser absorption spectroscopy. *Chem. Eng. Sci.* **1996**, *51*, 2607.
- (6) Hindle, F.; Carey, S.; Ozanyan, K.; Winterbone, D.; Clough, E.; McCann, H. Measurement of gaseous hydrocarbon distribution by a near infra-red absorption tomography system. *J. Electron. Imaging* **2001**, *10*, 593.
- (7) Aiouache, F.; Nic An tSaoir, M.; Kitagawa, K. Screening wall effects of a thin fluidized bed by near-infrared imaging. *Chem. Eng. J.* **2011**, *167*, 288–296.
- (8) Aiouache, F.; Oyama, O.; Kitagawa, K. Spatial near-infrared imaging of hydroxyl band coverage on ceria-based catalysts. *AIChE J.* **2006**, *52*, 1516–1521.
- (9) Paek, S.; Ahn, D.; Choi, H.; Kim, K.; Lee, M.; Yim, S.; Chunga, H.; Song, K.; Sohn, S. H. The performance of a trickle-bed reactor packed with a Pt/SDBC catalyst mixture for the CECE process. *Fusion Eng. Des.* **2007**, *82*, 2252.
- (10) Dyakowski, T.; Jaworski, A. Non-invasive process imaging—Principles and applications of industrial process tomography. *Chem. Eng. Technol.* **2003**, *26*, 697.
- (11) El-Fallah, J.; Boujana, S.; Dexpert, H.; Kiennemann, A.; Majerus, J.; Touret, O.; Villain, F.; Normand, F. Redox Processes on Pure Ceria and on Rh/CeO₂ Catalyst Monitored by X-ray Absorption. *J. Phys. Chem.* **1994**, *98*, 5522–5533.
- (12) Xu, G.; Sun, G.; Gao, S. Estimating radial voidage profiles for all fluidization regimes in circulating fluidized bed risers. *Powder Technol.* **2004**, *139*, 186–192.
- (13) Liu, X.; Xu, G.; Gao, S. Micro fluidized beds: wall effect and operability. *Chem. Eng. J.* **2008**, *137*, 302–307.
- (14) Roland, T. F.; Borysow, J.; Fink, M. Surface mediated isotope exchange reactions between water and gaseous deuterium. *J. Nucl. Mater.* **2006**, *353*, 193.
- (15) Crespi, F.; Bandera, A.; Donini, M.; Heidbreder, C.; Rovati, L. Non-invasive *in vivo* infrared laser spectroscopy to analyse endogenous oxy-haemoglobin, deoxy-haemoglobin, and blood volume in the rat CNS. *J. Neurosci. Methods* **2005**, *145*, 11–22.
- (16) Mujumdar, S.; Ramachandran, H. Imaging through turbid media using polarization modulation: dependence on scattering anisotropy. *Opt. Commun.* **2004**, *241*, 1–9.
- (17) Zhou, X.; Liu, X.; Jeffries, J. B.; Hanson, R. K. Development of a sensor for temperature and water concentration in combustion gases using a single tunable diode laser. *Meas. Sci. Technol.* **2003**, *14*, 1459.
- (18) Zhou, X.; Liu, X.; Jeffries, J. B.; Hanson, R. K. Development of a sensor for temperature and water concentration in combustion gases using a single tunable diode laser. *Meas. Sci. Technol.* **2003**, *14*, 1459–1468.
- (19) tSaoir, M. N.; Fernandes, D. L. A.; Sá, J.; McMaster, M.; Kitagawa, K.; Hardacre, C.; Aiouache, F. Visualization of water vapour flow in a packed bed adsorber by near-infrared diffused transmittance tomography. *Chem. Eng. Sci.* **2011**, *66*, 6407–6423.